Nonisothermal Model for Gas Separation Hollow-Fiber Membranes

D. T. Coker
Air Liquide, 3535 West 12th St., Houston, TX 77008

T. Allen and B. D. Freeman
Dept. of Chemical Engineering, North Carolina State University, Campus Box 7905, Raleigh, NC 27695

G. K. Fleming
Air Liquide, 305 Water Street, Newport, DE 19804

A model for multicomponent gas separation using hollow-fiber membrane modules is presented that explicitly accounts for heating or cooling inside membrane permeators due to gas expansion. The model permits simulation of countercurrent contacting with permeate purging (or sweep). The numerical approach permits rapid and stable solutions for cases with many components, even when the mixture contains components with widely varying permeability coefficients. Simulation results are presented for natural-gas sweetening, a commercially significant application, using polymer permeation properties similar to those of a high-performance polyimide. For some conditions, temperature decreases from the feed to residue end of the module by as much as 40°C. As CO_2 concentration in the feed increases or as stage cut increases, the temperature decrease from feed to residue increases. Relative to an isothermal case, expansion-driven cooling reduces stage cut at a given feed flow rate since gas permeability decreases with decreasing temperature. Neglect of expansion-driven cooling in natural-gas separation simulations can lead to large errors in estimating the amount of feed gas that can be treated to achieve a fixed residue composition. For 30% CO_2 feed concentration, if the effective membrane thickness is halved, only a 20% increase (rather than almost a factor of 2) in the amount of gas that can be treated per unit area is obtained due to the impact of expansion-driven cooling on gas flux.

Introduction and Background

Membrane-based gas separation is an important unit operation for the separation of air into high-purity nitrogen and oxygen-enriched air; removal of acid gases (such as CO_2 and H_2S) from natural gas; H_2 separation from mixtures with CO, CO_2, N_2, and hydrocarbons in a variety of petrochemical processes; and removal of organic vapors from air (Baker and Wijmans, 1994; Henis, 1994). Models are required to predict the performance of gas-separation modules for process design and optimization. In this study, hollow-fiber membrane modules are the focus of modeling efforts because of their widespread industrial use for membrane-based gas separation.

Excellent reviews of existing models of membrane gas permeators are presented by Kovvali et al. (1992) and by Lipscomb (1996). For highly simplified cases (such as perfectly mixed residue and feed), analytical solutions are available (Naylor and Backer, 1955; Smith et al., 1996; Weller and Steiner, 1950). Solutions for more complex cases can be obtained by series approximations or asymptotic analyses of the underlying differential equations governing mass transfer and pressure distribution in the module (Basaran and Auvil, 1988; Boucif et al., 1984; Krovvidi et al., 1992), by solving the governing differential equations directly as a two-point bound-

Correspondence concerning this article should be addressed to B. D. Freeman.

ary-value problem using shooting techniques (Kovvali et al., 1992), or by finite-element methods (Coker et al., 1998).

The models just described assume that the membrane module operates isothermally. However, the expansion of the residue (that is, high-pressure) gas in a membrane module to the lower pressure in the permeate stream can be accompanied by a change in temperature if the gas mixture is nonideal. The most common example of this effect is the well-known Joule-Thomsom cooling of gas passing through an adiabatic expansion valve. In this process, gas enthalpy remains constant as the gas expands from the high-pressure side of the valve to the low-pressure side, but pressure and specific volume change. For nonideal gases, this process can lead to the expanded gas being at either a higher or lower temperature than the compressed gas. Ideal gases do not undergo expansion-driven heating or cooling and therefore do not change temperature upon expansion in an adiabatic valve.

Limited studies of the effect of expansion-driven cooling have been reported for membranes. Rautenbach and Dahm used Joule-Thomson coefficients and a cross-flow mass-transfer model to analyze the influence of expansion-driven cooling of CO_2/CH_4 binary mixtures on temperature distribution in the module (Rautenbach and Dahm, 1987). The membrane was treated as a perfect insulator (that is, no exchange of energy between permeate and retentate streams as a result of conductive heat transfer). They concluded that the decrease in temperature resulting from this effect could cause as much as 20% variations in the permeate composition for the specific natural-gas separation cases they considered (due to changes in membrane permeability and selectivity with temperature). The magnitude of this effect was predicted to be greater for mixtures having larger differences between the activation energies of permeation of the two components.

Gorissen analyzed temperature changes in a cross-flow membrane module for binary gas mixtures (Gorissen, 1987). The membrane was also treated as a perfect insulator. Pressure changes in the membrane contactor were neglected, and the temperature dependence of permeability was not considered. Three gas mixtures were analyzed: (1) H_2/CO separation from a methane reformer; (2) O_2/N_2 separation; and (3) CO_2/CH_4 separation from biogas. The first two cases showed little change in temperature. The temperature increased by approximately 3°C for the H_2/CO separation, and decreased by about the same amount for the air-separation case. These results are in agreement with the sign of the Joule-Thomson coefficients for these gases. In the biogas case, however, large temperature changes were observed. The exit temperature from the module was calculated to be 30°C lower than the feed temperature for a 40 mole % CO_2 mixture with methane at a feed temperature of 40°C, a feed pressure of 70 bar, a permeate pressure of 2 bar, and a stage cut of 46%.

Cornelissen (1973) modeled heat transfer across an asymmetric spiral-wound membrane. Cornelissen suggested that the use of Joule-Thomson coefficients to estimate temperature changes in membrane units was incorrect since there is no separation as the gas mixture expands in a Joule-Thomson device and, in principle, the membrane permeation process is not necessarily isenthalpic. Based on a detailed analysis of heat transfer across a composite membrane, Cornelissen concluded that polymer membranes used commercially in membrane permeators were essentially infinitely conductive. This conclusion is contrary to the assumption used by Rautenbach and Dahm, and Gorissen. For CO_2/CH_4 separations in a spiral-wound separator, Cornelissen used a cross-flow model to calculate temperature differences in the module approaching 25°C at a stage cut of approximately 35%. In summary, the available literature suggests that expansion-driven cooling of gas mixtures relevant to natural-gas separations may lead to significant decreases in residue temperature relative to that of the feed. These models treat only binary mixtures, and none of them analytically addresses such effects in countercurrent hollow-fiber separation modules.

In this work, we present a multicomponent, countercurrent simulator for hollow-fiber membrane modules that incorporates coupled mass and energy balances to simulate permeator performance. The energy balance is derived by applying the thermal-energy balance (that is, the first law of thermodynamics) to the gas in the shell and bore of the hollow-fiber module. The differential energy balance is integrated to derive an appropriate macroscopic energy balance that is then applied to axial increments in the module. A detailed model of heat transfer across the fiber wall is incorporated to allow the membrane heat-transfer coefficient to be set to any value from 0 (perfect insulator) to infinity (perfectly conductive). An analysis of typical fiber properties is presented to guide selection of appropriate heat-transfer coefficient values. The energy balance is coupled to our previous multicomponent model (Coker et al., 1998), which solves the governing differential mass and pressure distribution in a hollow-fiber gas-separation permeator. A finite difference computational scheme, which does not rely on sometimes unstable, conventional shooting techniques, is used for numerical integration. Our numerical scheme permits rapid resolution of the differential mass, pressure, and temperature distribution equations even at very high stage-cuts (> 95%) for mixtures containing many components and wide variations in component permeances. The model is developed for countercurrent contacting patterns with or without permeate purging. Results are presented that demonstrate the effect of feed-gas composition and flowrate on temperature profiles for natural-gas separation.

Mathematical Model

Figure 1 depicts the flow configuration and internal structure of a typical hollow-fiber gas-separation module. The hol-

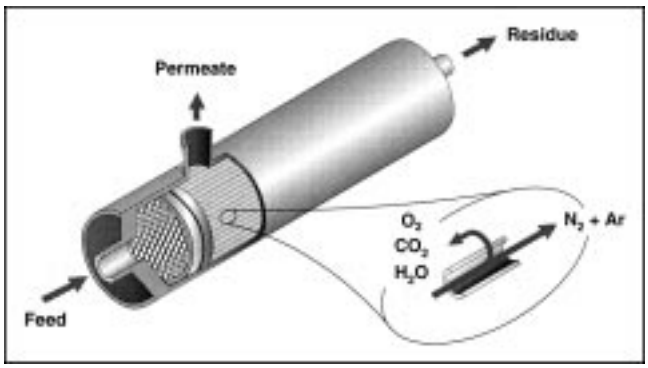

Figure 1. Hollow-fiber module showing component distribution in air separation.

low-fiber bundle is sealed on both ends by epoxy tube sheets and is contained inside a high-pressure housing. Feed gas can be introduced into the bore of the hollow fibers (as shown in Figure 1) or on the shell side of the module. For air separation, bore-side feed is commonly used commercially. For hydrogen and natural-gas separations, transmembrane pressures are much greater and shell-side feed is typical. Mechanically, the hollow fibers can sustain a much greater pressure difference across the fiber wall if the high-pressure gas is fed on the shell side rather than through the lumen of the fiber.

The principal assumptions underpinning the model are:

1. Shell-side pressure change is negligible.
2. Bore-side pressure change is given by the Hagen-Poiseuille equation (Bird et al., 1960).
3. The hollow fibers consist of a very thin membrane separation layer on a porous support. All mass-transfer resistance is confined to the separation membrane or the total membrane wall.
4. There is no axial mixing of shell- or lumen-side gases in the direction of bulk gas flow.
5. The gas on the shell side of the hollow fibers and in the lumen is in plug flow.
6. Deformation of the hollow fibers under pressure is negligible.
7. All fibers have uniform inner and outer radii as well as a uniform separation-layer thickness.
8. The membrane module is operated at steady state.
9. The Redlich-Kwong equation of state adequately describes the pressure–volume–temperature (PVT) properties of the gas mixture (Reid et al., 1987).
10. The module is adiabatic.
11. Axial convective heat transfer dominates axial conductive heat transfer except at the sealed end of the hollow fibers.
12. Effects of viscous dissipation and reversible work are negligible or offset one another.
13. No condensation occurs by the expansion-driven cooling process.

As explained in more detail in the following sections, the hollow-fiber module is divided into a series of N stages in the axial direction, and mass and energy balances are enforced in each section. This procedure is formally equivalent to using first-order finite differences to develop a set of coupled difference equations from the differential mass balances for this problem. The mass and pressure-distribution equations have been published previously (Coker et al., 1998; Lipscomb, 1996; Pan, 1986).

Energy Balance

The steady-state, point thermal energy balance for gas on the shell or bore side of the fibers is (Whitaker, 1985):

$$\rho \boldsymbol{v} \cdot \nabla H = -\nabla \cdot q + \boldsymbol{v} \cdot \nabla P + \overline{\nabla \boldsymbol{v}} : \bar{\boldsymbol{\tau}}, \qquad (1)$$

where H is enthalpy per unit mass of gas; ρ is gas density; $\boldsymbol{v}$ is gas velocity; P is gas pressure; and $\bar{\boldsymbol{\tau}}$ is the stress tensor. The net flux of energy per unit volume of gas due to conduction is $-\nabla \cdot q$; the net energy flux per unit volume due to convection is $\rho \boldsymbol{v} \cdot \nabla H$; the rate of reversible work per unit volume is $\boldsymbol{v} \cdot \nabla P$; and the rate of irreversible work per unit volume of gas (that is, viscous dissipation) is $\overline{\nabla \boldsymbol{v}} : \bar{\boldsymbol{\tau}}$. To obtain the macroscopic thermal energy balance used to model heat transfer in each section of the membrane module, Eq. 1 is integrated over the shell-side control volume and the tube-side control volumes shown by the dashed lines in Figure 2. The integrals are taken over the volume of gas contained in the shell-side control volume element of length Δz and over the tube-side control volume element of length Δz. The integration of the energy balance is performed over a control volume V_1 that represents either the shell-side or tube-side control volume. Afterwards, the results are specialized for the tube side and shell side of each element of length Δz. Then, the shell- and tube-side energy balances of each element are combined to form a set of nonlinear algebraic equations that are solved to calculate the temperature profile in the module.

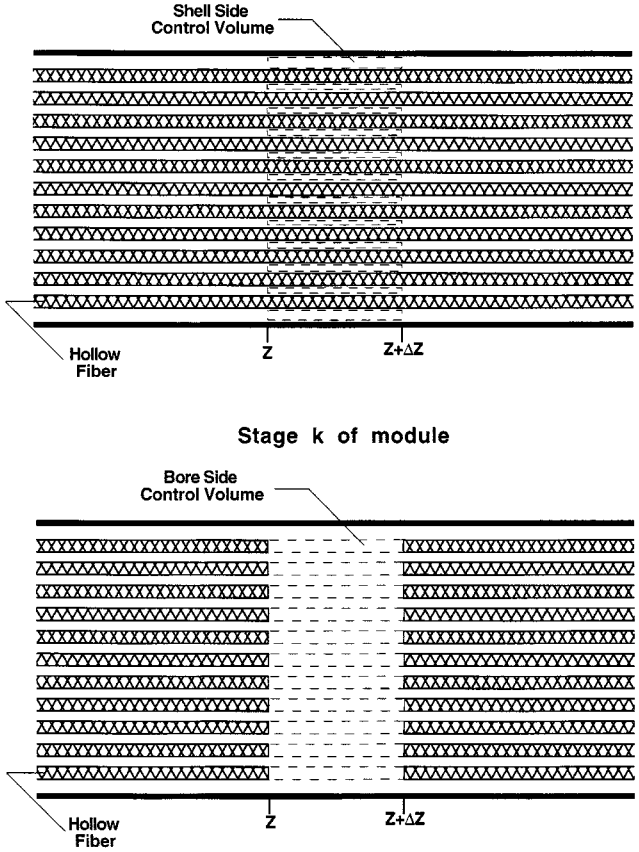

Figure 2. Cross section of hollow-fiber module and control volumes for energy balance.

The integral of Eq. 1 over the control volume V_1 is

$$\int_{V_1} \rho \boldsymbol{v} \cdot \nabla H \, dV = -\int_{V_1} \nabla \cdot q \, dV + \int_{V_1} \left[\boldsymbol{v} \cdot \nabla P + \overline{\nabla \boldsymbol{v}} : \bar{\boldsymbol{\tau}} \right] dV. \qquad (2)$$

Applying the divergence theorem to the convective and conductive heat-transfer terms yields:

$$\int_{A_1} \rho H \boldsymbol{v} \cdot n \, dA = -\int_{A_1} q \cdot n \, dA + \int_{V_1} \left[\boldsymbol{v} \cdot \nabla P + \overline{\nabla \boldsymbol{v}} : \bar{\boldsymbol{\tau}} \right] dV, \qquad (3)$$

where A_1 is the area of the control volume V_1, and n is the unit normal, which is directed outward from the surface of the control volume. The last integral in Eq. 3 represents the contributions of reversible work and viscous dissipation to the thermal-energy balance. As demonstrated in Appendix A, these two terms may be significant for typical flow rates of gas in hollow fibers. However, the terms are opposite in sign and, for an ideal gas, cancel each other. For nonideal gas mixtures, such as the CO_2/CH_4 mixtures considered in this study, these two terms do not cancel perfectly. However, for most of the cases considered in this study, the net effect is expected to be small, so these terms are neglected in the remainder of this analysis. With this assumption, the thermal-energy balance over the control volume becomes

$$\int_{A_1} \rho H \boldsymbol{v} \cdot \boldsymbol{n}\, dA = -\int_{A_1} \boldsymbol{q} \cdot \boldsymbol{n}\, dA. \tag{4}$$

The integrals in Eq. 4 can be written as a sum of integrals over the faces of the control volume:

$$\int_{A_1} \rho H \boldsymbol{v} \cdot \boldsymbol{n}\, dA = \sum_{i=1}^{m} \int_{A_{1,i}} \rho H \boldsymbol{v} \cdot \boldsymbol{n}\, dA, \tag{5}$$

where m is the number of faces or sides of the control volume. The bulk or mixing cup enthalpy per unit mass on face i of the control volume is defined as follows:

$$\hat{H}_i \equiv \frac{\int_{A_{1,i}} \rho H \boldsymbol{v} \cdot \boldsymbol{n}\, dA}{\int_{A_{1,i}} \rho \boldsymbol{v} \cdot \boldsymbol{n}\, dA}. \tag{6}$$

The mass flow rate through face i of the control volume, w_i, is defined as

$$w_i \equiv \int_{A_{1,i}} \rho \boldsymbol{v} \cdot \boldsymbol{n}\, dA. \tag{7}$$

The heat flow through face i of the control volume due to conduction, $\dot{Q}_i$, is defined as

$$\dot{Q}_i \equiv -\int_{A_{1,i}} \boldsymbol{q} \cdot \boldsymbol{n}\, dA. \tag{8}$$

Combining Eqs. 4–8 yields:

$$\sum_{i=1}^{m} w_i \hat{H}_i = \sum_{i=1}^{m} \dot{Q}_i. \tag{9}$$

Heat flow due to conduction in the axial direction is much less important than convective heat transfer in the axial direction for simulation conditions of industrial interest. This assumption is valid for flow in tubes if the following criterion is met (Whitaker, 1985):

$$RePr\frac{L}{D} \gg 1, \tag{10}$$

where Re is the Reynolds number, defined for tubeside feed to be $Re = D_i\langle v\rangle/\nu$; Pr is the Prandtl number; D_i is the inside diameter of the fibers; $\langle v\rangle$ is the average axial velocity of gas through a fiber; and ν is the gas kinematic viscosity. For a tube-side air-separation membrane containing 500,000 fibers of inside diameter 150 μm and operating at a total feed flow rate of 1416 m^3(STP)/hour (50,000 SCFH), the maximum average velocity in a fiber is 44.5 m/s. The kinematic viscosity of air at ambient conditions is 1.3×10^{-5} m^2/s (Whitaker, 1985), so the Reynolds number will be approximately 510. The Prandtl number of air at ambient conditions is 0.72 (Whitaker, 1985). If the active fiber length, L, is 0.8 m, then $RePr(L/D) \approx 2\times10^6$, which clearly satisfies Eq. 10. In fact, feed flow rates many orders of magnitude lower would also satisfy Eq. 10, so the assumption of negligible axial conduction is satisfactory everywhere in the module except at points where gas flow rate is zero, such as the closed end of the fibers. At such points, there is no heat transfer since the module is adiabatic in this analysis. A similar analysis of shell-side feed for fiber packings of 50% (typical of industrial modules) suggests that this approximation is also valid for shell-side feed flow. Additionally, the approximation should also be valid for shell- or tube-side permeate flow under typical industrial membrane contactor operating conditions. Therefore, Eq. 9, the energy balance over a control volume of length Δz, is simplified to

$$\sum_{i=1}^{m} w_i \hat{H}_i = \dot{Q}_{\text{mem}} \tag{11}$$

where $\dot{Q}_{\text{mem}}$ is the net rate of conductive energy flow across the hollow-fiber wall.

In the derivation that follows, it will be more convenient to refer to a single element of the membrane module as shown in Figure 3A. Figure 3B shows the entire membrane module divided into N elements. When Eq. 11 is applied to the residue (or feed) side of the membrane element shown in Figure 3A, the result is

$$\hat{H}^L_{k+1} L_{k+1} = \hat{H}^L_k L_k + \hat{H}^L_{k+1} \sum_{j=1}^{K} \dot{m}_{j,k} - \dot{Q}_{\text{mem}_R}, \tag{12}$$

where L_{k+1} is the residue flow rate to stage k from stage $k+1$; L_k is the total residue flow rate leaving stage k; $\dot{Q}_{\text{mem}_R}$ is the net rate of conductive heat flow across the fiber wall into the residue control volume; K is the number of components in the mixture; and $\dot{m}_{j,k}$ is the mass flow rate of component j that leaves the residue side of stage k due to permeation across the membrane. In Eq. 12, the gas leaving the residue due to permeation through the fiber wall is assigned the enthalpy (per unit mass) of the feed stream entering stage k, $\hat{H}^L_{k+1}$. One could also set the thermodynamic properties of the gas permeating across the membrane wall to that of the residue gas leaving the stage. However, when the size of stage k, Δz, is small, there is no significant difference in the calculated temperature profile using either method to evaluate the enthalpy of the gas permeating through the fiber wall. Applying Eq. 11 to stage k gives

$$\hat{H}^L_{k+1} L_{k+1} + \hat{H}^V_{k-1} V_{k-1} = \hat{H}^L_k L_k + \hat{H}^V_k V_k, \tag{13}$$

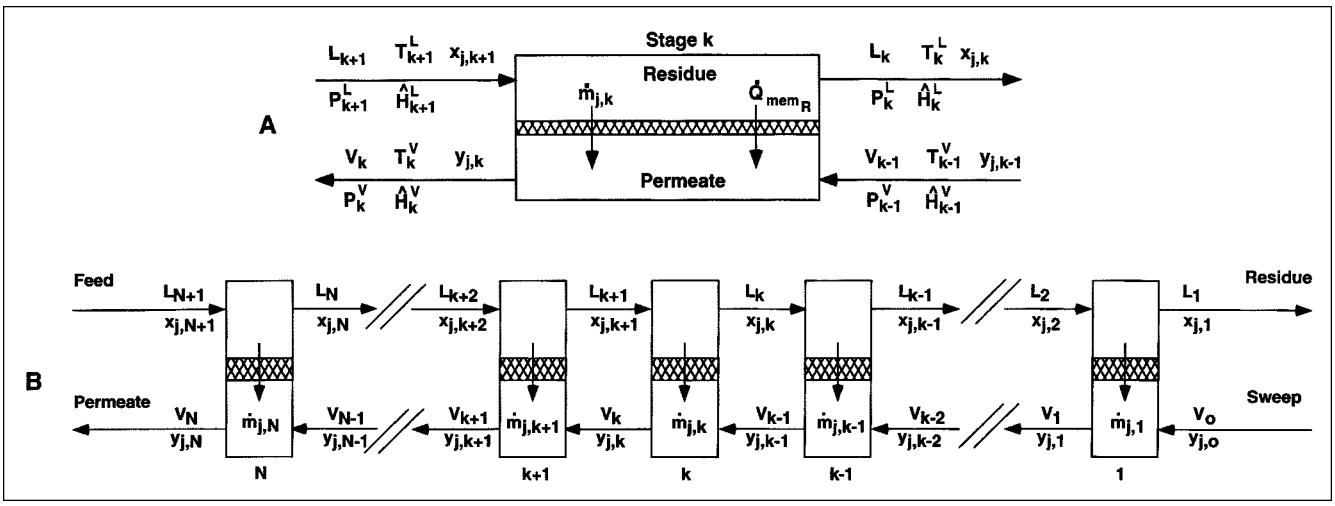

Figure 3. (A) Stage *k* of membrane module; (B) membrane module divided into *N* stages.

where V_{k-1} is the permeate flow rate entering stage k, and V_k is the permeate flow rate leaving stage k.

The mass flow rate of component j in the gas mixture permeated on stage k is given by Barrer (1942), Ghosal and Freeman (1994), and Graham (1866)

$$\dot{m}_{j,k} = Q_j \Delta A_k \left(P_k^L x_{j,k} - P_k^V y_{j,k} \right), \tag{14}$$

where Q_j is the permeance (that is, permeability divided by active layer membrane thickness) of component j; and P_k^L and P_k^V are the residue and permeate pressures on stage k; ΔA_k is the area available for mass transfer on stage k, and is defined as follows:

$$\Delta A_k = \frac{2\pi R_o L N_f}{N}, \tag{15}$$

where L is the active (or permeating) length of the hollow fibers in the module; N_f is the number of fibers in the module; N is the number of increments into which the module is divided; and R_o is the outer radius of the hollow fiber. The algorithm for determining N was presented previously (Coker et al., 1998).

The enthalpies appearing in Eqs. 12 and 13 are evaluated as follows:

$$\begin{aligned} \hat{H}_{k+1}^L &= H_{k+1}^{O,L} - \epsilon_{k+1}^L \\ \hat{H}_{k-1}^V &= H_{k-1}^{O,V} - \epsilon_{k-1}^V \\ \hat{H}_k^L &= H_k^{O,L} - \epsilon_k^L \\ \hat{H}_k^V &= H_k^{O,V} - \epsilon_k^V \end{aligned} \tag{16}$$

where $H_{k+1}^{O,L}$, $H_k^{O,L}$, $H_{k-1}^{O,V}$, and $H_k^{O,V}$ are the ideal gas enthalpies (J/kmol) of the residue stream entering and leaving stage k and the ideal gas enthalpies of the permeate streams entering and leaving stage k, respectively. ϵ_{k+1}^L, ϵ_k^L, ϵ_{k-1}^V, and ϵ_k^V are enthalpy departure functions (J/kmol) of the residue stream entering and leaving stage k and enthalpy departure functions of the permeate stream entering and leaving stage k, respectively. The enthalpy departure functions give the enthalpy change of the stream upon depressurization from process pressure to zero pressure (that is, the ideal gas state). Using the feed stream to stage k as the reference, the enthalpies appearing in Eq. 16 may be evaluated explicitly as shown below (Prausnitz, 1969; Smith and Ness, 1987):

$$\begin{aligned} \hat{H}_{k+1}^L &= 0 - \epsilon_{k+1}^L \\ \hat{H}_{k-1}^V &= \sum_{j=1}^{K} y_{j,k-1} \int_{T_{k+1}^L}^{T_{k-1}^V} C_{p,j}^o dT - \epsilon_{k-1}^V \\ &= \overline{C}_{p,k-1}^V \left(T_{k-1}^V - T_{k+1}^L \right) - \epsilon_{k-1}^V \\ \hat{H}_k^L &= \sum_{j=1}^{K} x_{j,k} \int_{T_{k+1}^L}^{T_k^L} C_{p,j}^o dT - \epsilon_k^L = \overline{C}_{p,k}^L \left(T_k^L - T_{k+1}^L \right) - \epsilon_k^L \\ \hat{H}_k^V &= \sum_{j=1}^{K} y_{j,k} \int_{T_{k+1}^L}^{T_k^V} C_{p,j}^o dT - \epsilon_k^V = \overline{C}_{p,k}^V \left(T_k^V - T_{k+1}^L \right) - \epsilon_k^V, \end{aligned} \tag{17}$$

where the average ideal gas heat capacities of the gas mixtures (J/(kmol K)) in the permeate stream entering stage k, leaving stage k, and in the residue stream leaving stage k are $\overline{C}_{p,k-1}^V$, $\overline{C}_{p,k}^V$, and $\overline{C}_{p,k}^L$, respectively. The heat capacities are calculated using the power-series representation for the temperature dependence of heat capacity in the monograph by Lide and Kehiaian (1994). For example, the heat capacity of the permeate stream entering stage k is calculated as follows:

$$\begin{aligned} \overline{C}_{p,k-1}^V &= \sum_{j=1}^{K} \frac{y_{j,k-1}}{\left(T_{k-1}^V - T_{k+1}^L \right)} \sum_{i=1}^{5} \int_{T_{k+1}^L}^{T_{k-1}^V} A_{i,j} T^{i-1} dT \\ &= \sum_{j=1}^{K} \frac{y_{j,k-1}}{\left(T_{k-1}^V - T_{k+1}^L \right)} \sum_{i=1}^{5} \frac{A_{i,j}}{i} \left[\left(T_{k-1}^V \right)^i - \left(T_{k+1}^L \right)^i \right], \end{aligned} \tag{18}$$

where $A_{i,j}$ is the ith coefficient in the power-series representation of the ideal gas heat capacity of component j.

We use the Redlich-Kwong equation of state to evaluate the enthalpy departure functions in Eq. 17. This model or variations of it are widely used in the gas processing industry, and its properties are well understood. For this equation of state, the results are (Reid et al., 1987)

$$\epsilon_{k+1}^L = RT_{k+1}^L - P_{k+1}^L \hat{V}_{k+1}^L + \frac{3}{2}\frac{a_{k+1}^L}{b_{k+1}^L \left(T_{k+1}^L\right)^{1/2}} \ln\left[1+\frac{b_{k+1}^L}{\hat{V}_{k+1}^L}\right]$$

$$\epsilon_{k-1}^V = RT_{k-1}^V - P_{k-1}^V \hat{V}_{k-1}^V + \frac{3}{2}\frac{a_{k-1}^V}{b_{k-1}^V \left(T_{k-1}^V\right)^{1/2}} \ln\left[1+\frac{b_{k-1}^V}{\hat{V}_{k-1}^V}\right]$$

$$\epsilon_k^L = RT_k^L - P_k^L \hat{V}_k^L + \frac{3}{2}\frac{a_k^L}{b_k^L \left(T_k^L\right)^{1/2}} \ln\left[1+\frac{b_k^L}{\hat{V}_k^L}\right]$$

$$\epsilon_k^V = RT_k^V - P_k^V \hat{V}_k^V + \frac{3}{2}\frac{a_k^V}{b_k^V \left(T_k^V\right)^{1/2}} \ln\left[1+\frac{b_k^V}{\hat{V}_k^V}\right], \qquad (19)$$

where $\hat{V}_{k+1}^L$, $\hat{V}_k^L$, $\hat{V}_{k-1}^V$, and $\hat{V}_k^V$ are the specific volumes of the residue stream entering and leaving stage k and the specific volumes of the permeate streams entering and leaving stage k, respectively. The Redlich-Kwong mixture coefficients for each stream are given by the a and b coefficients in Eq. 19. The mixing rules for a and b as well as correlations to determine them based on the critical temperature and pressure of the components in the mixture are well known (Reid et al., 1987). If another equation of state provides a better description of the gas-mixture thermodynamic properties, one could evaluate the enthalpy departure functions for the desired equation of state according to published methods (Reid et al., 1987).

Combining Eqs. 13 and 17 gives

$$T_k^V = T_{k+1}^L + \frac{1}{V_k \overline{C}_{p,k}^V}\Big[V_{k-1}\overline{C}_{p,k-1}^V\left(T_{k-1}^V - T_{k+1}^L\right) - L_k \overline{C}_{p,k}^L\left(T_k^L - T_{k+1}^L\right) - \delta_k\Big], \qquad (20)$$

where δ_k is

$$\delta_k = L_{k+1}\epsilon_{k+1}^L + V_{k-1}\epsilon_{k-1}^V - V_k\epsilon_k^V - L_k\epsilon_k^L. \qquad (21)$$

To complete the problem formulation, a model for heat transfer across the fiber wall is required. In this model, we assume that the gas permeating the membrane does so isenthalpically. In this limit, the rate of heat transfer from the residue face of the membrane to the bulk residue gas is equal to the absolute value of the rate of heat transfer from the permeate face of the membrane to the bulk permeate gas. The following model for the conductive heat flow across the membrane fiber wall is used

$$\dot{Q}_{\mathrm{mem}_R} = U_o \Delta A_k\left(T_k^V - T_k^L\right), \qquad (22)$$

where U_o is the overall heat-transfer coefficient. If heat is transferred from the residue to the permeate stream, $\dot{Q}_{\mathrm{mem}_R}$ is less than zero, and greater than zero if the net flow of heat is from the permeate to the residue stream. Appendix B provides detailed procedures to estimate the value of U_o. In all of the simulation results considered in this work, U_o is set to a value of 1000 W/(m^2 K), which essentially makes the membrane infinitely conductive. The results in Appendix B suggest that, at typical operating conditions, gas separation membranes in current commercial applications are essentially infinitely conductive.

Formulation of energy balance as a tridiagonal matrix

Inserting Eq. 22 into Eq. 12 and using Eq. 17 gives

$$T_k^L = \alpha_k^L T_{k+1}^L + \left(1-\alpha_k^L\right)T_k^V + \gamma_k^L, \qquad (23)$$

where

$$\alpha_k^L = \left[1+\frac{U_o \Delta A_k}{L_k \overline{C}_{p,k}^L}\right]^{-1} \qquad (24)$$

and

$$\gamma_k^L = \frac{\alpha_k^L}{\overline{C}_{p,k}^L}\left(\epsilon_k^L - \epsilon_{k+1}^L\right). \qquad (25)$$

Equation 23 is an energy balance for the residue side of stage k in the hollow-fiber module. In a similar fashion, the residue-side energy balance for stage $k-1$ may be written as follows:

$$T_{k-1}^L = \alpha_{k-1}^L T_k^L + \left(1-\alpha_{k-1}^L\right)T_{k-1}^V + \gamma_{k-1}^L. \qquad (26)$$

An expression for the temperature of the permeate stream leaving stage k is obtained by substituting Eq. 23 into Eq. 20 to eliminate T_k^L. The result is

$$T_k^V = \alpha_k^V T_{k-1}^V + \left(1-\alpha_k^V\right)T_{k+1}^L + \gamma_k^V, \qquad (27)$$

where

$$\alpha_k^V = \frac{V_{k-1}\overline{C}_{p,k-1}^V}{V_k \overline{C}_{p,k}^V + \left(1-\alpha_k^L\right)L_k \overline{C}_{p,k}^L} \qquad (28)$$

and

$$\gamma_k^V = \frac{-\delta_k - \alpha_k^L L_k\left(\epsilon_k^L - \epsilon_{k+1}^L\right)}{V_k \overline{C}_{p,k}^V + \left(1-\alpha_k^L\right)L_k \overline{C}_{p,k}^L}. \qquad (29)$$

Combining Eqs. 23, 26, and 27 gives the desired result:

$$\Delta_k T_{k+1}^L + \Phi_k T_k^L + \Psi_k T_{k-1}^L = E_k, \qquad (30)$$

where

$$\Delta_k = \alpha_k^L + \left(1-\alpha_k^L\right)\left(1-\alpha_k^V\right) \tag{31}$$

$$\Phi_k = -1-\alpha_{k-1}^L \Psi_k \tag{32}$$

$$\Psi_k = \alpha_k^V \frac{\left(1-\alpha_k^L\right)}{\left(1-\alpha_{k-1}^L\right)} \tag{33}$$

and

$$E_k = \gamma_{k-1}^L \Psi_k - \gamma_k^L - \gamma_k^V\left(1-\alpha_k^L\right). \tag{34}$$

When Eq. 30 is written for each stage, the resulting set of coupled nonlinear equations can be organized into a tridiagonal matrix as shown below:

$$\begin{bmatrix} \Phi_1 & \Delta_1 & & & & \\ \Psi_2 & \Phi_2 & \Delta_2 & & & \\ \hline & \Psi_k & \Phi_k & \Delta_k & & \\ \hline & & \Psi_{N-1} & \Phi_{N-1} & \Delta_{N-1} & \\ & & & \Psi_N & \Phi_N & \end{bmatrix} \begin{bmatrix} T_1^L \\ T_2^L \\ \hline T_k^L \\ \hline T_{N-1}^L \\ T_N^L \end{bmatrix} = \begin{bmatrix} E_1 \\ E_2 \\ \hline E_k \\ \hline E_{N-1} \\ E_N - \Delta_N T_{N+1}^L \end{bmatrix}. \tag{35}$$

In the last row, T_{N+1}^L is the feed temperature, which is known. If the simulation is to be run with a permeate sweep stream, then its flow rate, V_o, and temperature, T_o^V, are presumed to be specified. For the first stage ($k=1$) at the residue end of the fibers, the coefficient E_1 is modified as follows when a permeate sweep is used:

$$E_1 = -\gamma_1^L - \gamma_1^V \beta_1^L - \alpha_1^V \beta_1^L T_o^V. \tag{36}$$

Tridiagonal matrices can be solved very efficiently using the Thomas algorithm (King, 1980). The solution to Eq. 35 yields the residue temperature profile throughout the module.

To begin the calculation, the temperature of the module is set equal to the feed temperature. Then the number of axial increments, mass, and pressure distributions are calculated using the procedures described previously (Coker et al., 1998). Afterwards, all coefficients in Eq. 35 are evaluated at the feed temperature, and Eq. 35 is solved using the Thomas algorithm to generate a new temperature profile. The temperature profile influences the mass distribution in the module because permeabilities may be set to depend on temperature and because the pressure distribution in the bore of the fibers depends on temperature. With the new temperature profile, the mass and pressure distributions are recalculated. Based on the updated mass and pressure distribution, the temperature profile is updated. This iterative, successive substitution procedure is repeated until the flow rates meet the following criteria:

$$\left|\frac{\Delta L_1}{L_1}\right| < 10^{-8}$$
$$\left|\frac{\Delta V_{N+1}}{V_{N+1}}\right| < 10^{-8} \tag{37}$$

and until the energy balance around the entire module meets the following criterion:

$$\left|\frac{\Delta H}{H_{N+1}}\right| < 10^{-8}. \tag{38}$$

In Eq. 37, ΔL_1 and ΔV_{N+1} are the changes in total residue flow and total permeate flow from one iteration to the next. In Eq. 38, ΔH is the difference between the enthalpy of the feed stream and that of the residue and permeate streams, and H_{N+1} is the enthalpy of the feed stream. In practice, we find that the energy-balance criterion is usually met before the flow rate criteria are satisfied.

The nested successive substitution method we have outlined could, in principle, suffer from numerical stability problems due to its limited radius of convergence. We elected to use this numerical-solution strategy because it was the simplest extension of our earlier simulator development for isothermal gas separations (Coker et al., 1998). For the cases that we considered, we did not have any convergence difficulties over the range of operating conditions explored, which encompass the window of practical operation of industrial separators. One could, of course, use more sophisticated and elegant numerical techniques, such as the Newton-Raphson approach, to establish an inherently more stable solution methodology. However, this approach would require more computation overhead. For the results presented in this article, typical countercurrent simulations require no more than 5–50 iterations to achieve convergence, and such a case requires a few seconds when the simulator is run using a personal computer. Also, we verified that the number of axial increments used in the simulations was sufficient to make the results independent of the number of axial increments.

Once the residue temperature profile is converged, the permeate temperature profile can be calculated directly from Eq. 23 as follows:

$$T_k^V = \frac{T_k^L - \alpha_k^L T_{k+1}^L - \gamma_k^L}{\left(1-\alpha_k^L\right)}. \tag{39}$$

Results and Discussion

Natural-gas treatment

Results are presented for both binary and multicomponent cases with process conditions similar to those used in industrial natural-gas treatment, where CO_2 is removed from a mixture of methane and other hydrocarbons to adjust the heating value of the natural gas (Bhide and Stern, 1993a,b).

Table 1. Module and Process Simulation Parameters

Feed	Shell-side
Feed pressure (bara)	59.6
Permeate pressure (bara)	1.70
Feed temperature (°C)	50
Fiber outside diameter (μm)	300
Fiber inside diameter (μm)	150
Fiber length (m)	1
Fiber pot length (m)	0.1
Number of fibers	500,000
Active membrane area (m^2)*	377

*Active membrane area is calculated as π (fiber outside diameter)(fiber length − 2 (fiber pot length)) (number of fibers). This module configuration has the active separating layer on the exterior of the fiber. The fibers are potted on each end.

Table 1 gives the module and process conditions used in these simulations. The permeance values used for the components in the model natural-gas mixtures are presented in Table 2. The values in this table correspond to those reported for a polyimide prepared from 3,3′,4,4′-biphenyltetracarboxylic dianhydride and 4,4′-diaminodiphenyl ether if the effective separation layer thickness is 0.1 μm (Haraya et al., 1986). This polyimide is a high performance material with good combinations of permeability and selectivity for these gases. Haraya et al. also report the temperature dependence of permeability coefficients for a variety of gases in this polymer, and this information is useful for the simulations, as temperature can have a significant impact on gas permeability coefficients.

In these simulations, we use pressure-independent permeability coefficients and activation energy values. More sophisticated models of the pressure dependence of permeability (Ghosal and Freeman, 1994) and activation energy (Koros et al., 1979), as well as the effect of gas mixture composition on permeation properties, are available and can easily be implemented if desired. However, our goal is to develop a framework for modeling the effect of expansion-driven cooling of gas mixtures on separation performance of hollow-fiber contactors and then explore predictions of the model for simplified cases. Consequently, we have only considered the most basic model (that is, pressure and composition independent permeability and activation energy values) to describe selective gas transport through thin polymer membranes. In this same spirit, we use gas viscosity values at ambient pressure and the feed temperature, and do not allow viscosity to vary with pressure or temperature. We use standard mixing rules to estimate the effect of gas composition on gas viscosity (Bird et al., 1960; Coker et al., 1998) and allow gas viscosity to change with composition along the fibers. Gas viscosity is important in determining the pressure drop in the bore of the fibers.

Table 2. Permeance Values at Feed Temperature (50°C) for Natural-Gas Separation

Component	Permeance (GPU)*
CO_2	22.7
CH_4	0.7
N_2	4.4
C_2H_6	0.75
C_3H_8	0.009

*1 GPU = 10^{-6} cm^3 (STP)/(cm^2·s·cm Hg) = 7.501×10^{-12} m^3(STP)/(m^2·s·Pa) = 3.346×10^{-13} kmol/(m^2·s·Pa).

Figure 4 presents pure gas permeability coefficients and activation energies of permeation of this polyimide at 25°C as a function of penetrant critical volume, V_c, a convenient measure of penetrant size. The sensitivity of the permeability coefficient to temperature is given by an Arrhenius expression:

$$P_A = P_o e^{-E_p/(RT)}, \tag{40}$$

where E_p is the activation energy of permeation and P_o is a temperature-independent front factor.

To provide an indication of the influence of temperature on gas permeation properties of the penetrants in Figure 4, Eq. 40 was used to calculate the temperature change required to double the permeability coefficients. These results are presented in Figure 5 as a function of penetrant size. In general, the smaller penetrants, which have lower activation energies of permeation, require the largest temperature change to double permeability. As penetrant size increases, activation energy increases and, in turn, the temperature change required to double permeability decreases. This result indicates that not only will membrane permeability coefficients change with temperature, but that selectivity values (that is, ratios of permeability coefficients) will also change with temperature. For the natural-gas separations considered in this study (that is, CO_2 removal from mixtures with methane and other hydrocarbons), selectivity increases as temperature decreases because the most permeable penetrant (CO_2 in this case) has the lower activation energy.

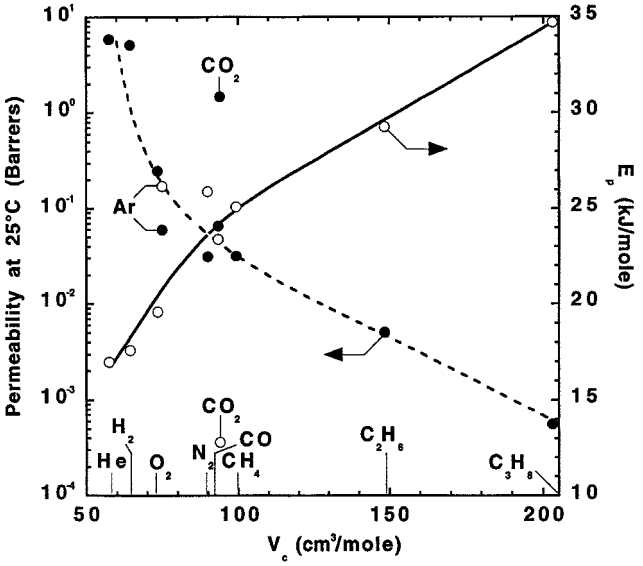

Figure 4. Permeability and activation energy as a function of penetrant critical volume, V_c, in the polyimide prepared from 3,3′,4,4′-biphenyltetracarboxylic dianhydride and 4,4′-diaminodiphenyl ether (Haraya et al., 1986).

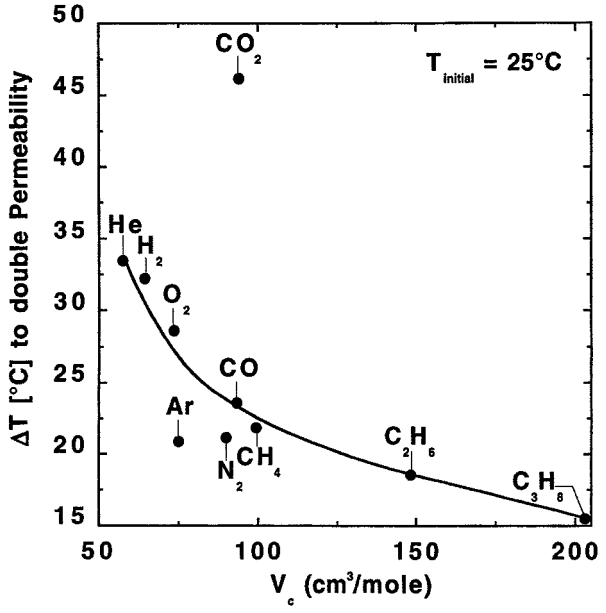

Figure 5. Temperature change required to double permeability coefficient as a function of penetrant critical volume.

The permeability properties are those of the polyimide shown in Figure 4.

CO_2/CH_4 Separation: temperature-independent permeability coefficients

Figure 6 shows the process conditions used for simulation of CO_2 removal from natural gas using membranes (Bhide and Stern, 1993a,b). The simplest model scenario for natural-gas treatment is the removal of CO_2 from mixtures with methane. In this regard, Figure 6A gives the process conditions used for our binary simulations of natural-gas sweetening. While feed-gas conditions (temperature, pressure, and composition) may vary significantly from one gas source to another, we use typical feed temperature and pressure values and do not vary these parameters. The gas composition, which has a large impact on gas thermodynamic properties and therefore expansion-driven temperature changes, is varied over ranges typical for CO_2 contents in natural-gas wells. The module parameters (number of fibers, fiber geometry, flow pattern) are typical for hollow-fiber membranes used for this application.

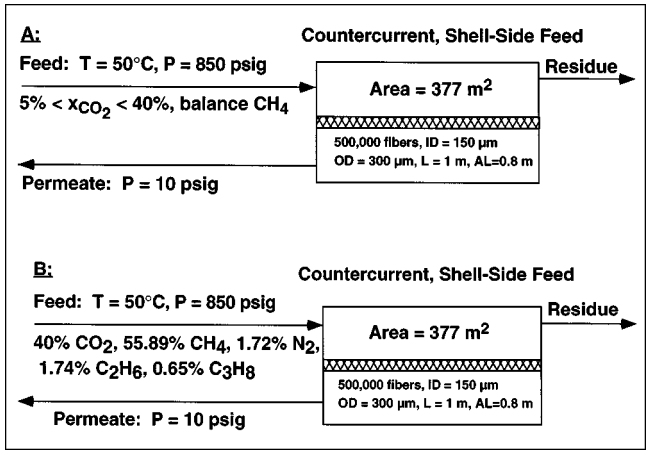

Figure 6. Flowsheets for natural-gas simulations.

(A) Model binary case (Bhide and Stern, 1993a). (B) Multicomponent case. *AL* = active fiber length, which is the total fiber length, *L*, minus twice the pot length, 0.1 m in this case.

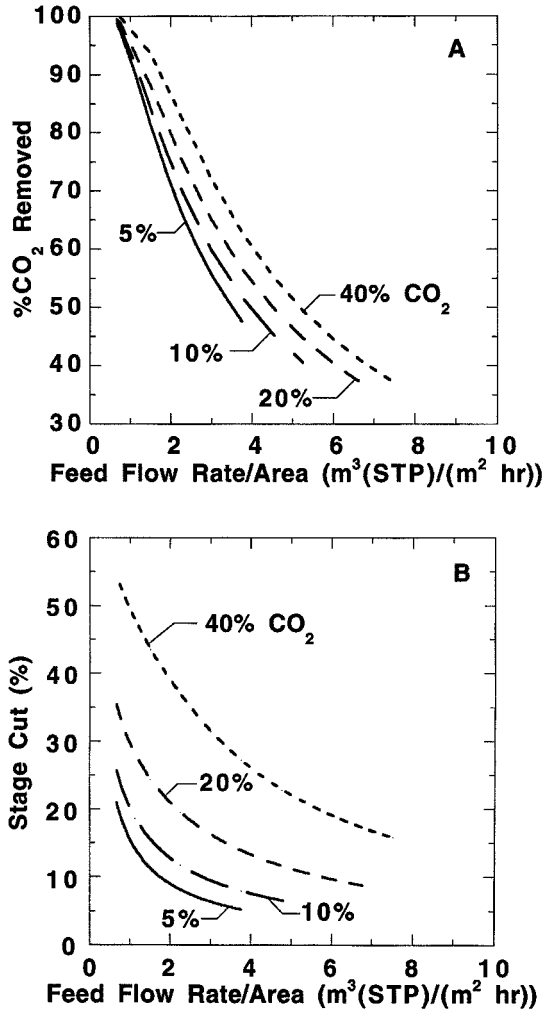

Figure 7. Effect of feed flow rate and feed composition of CO_2 on (A) fractional CO_2 removal and (B) stage cut in binary natural-gas separation.

Figure 7 reports the influence of feed flow rate and CO_2 feed composition on fractional CO_2 removal and stage cut. In these results, only binary mixtures (CO_2 and CH_4) are considered. Furthermore, to isolate the effect of temperature changes due entirely to expansion-driven cooling, the membrane permeation properties are taken to be constant at the values characteristic of the feed temperature, 50°C. From Figure 7A, as feed flow rate increases, the fraction of CO_2 removed from the feed decreases, consistent with the shorter contact time of the high-pressure residue gas with the active membrane area at higher feed flow rates. At a fixed flow

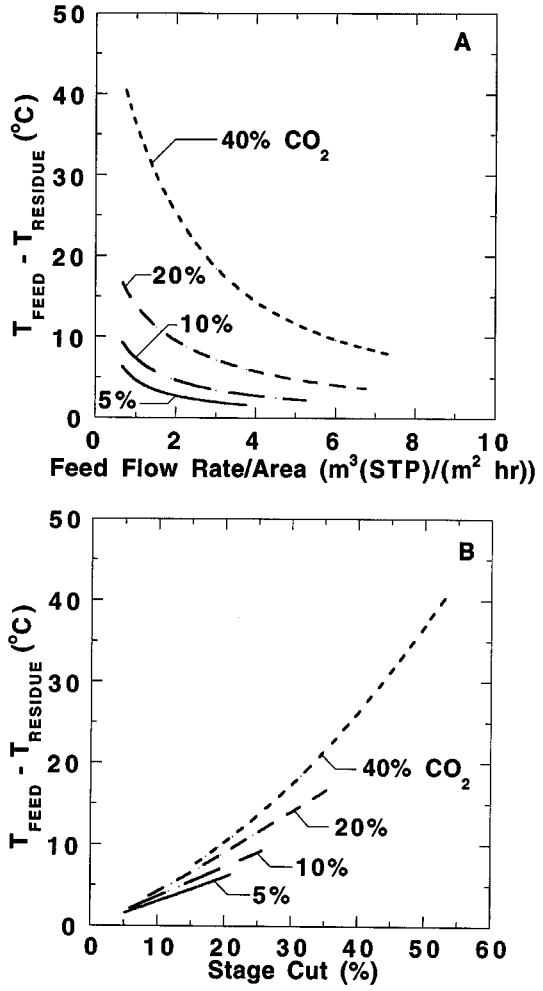

Figure 8. Temperature difference between feed and residue stream as a function of CO_2 composition in the feed and (A) feed flow rate per unit membrane area and (B) stage cut.

The simulation conditions are those for the binary natural-gas case.

rate, the amount of CO_2 removed from the feed gas increases as the concentration of CO_2 in the feed increases. This result is consistent with the increased driving force for CO_2 transport from the high-pressure residue stream to the low-pressure permeate stream as CO_2 feed concentration increases. Figure 7B presents the impact of feed concentration and flow rate on stage cut. Stage cut is the ratio of permeate flow rate to feed flow rate. Based on the results in Figure 7B, stage cut follows qualitatively the same trend as fractional CO_2 removal. At higher feed flow rates, a smaller fraction of the gas is transferred from the residue to the permeate stream. Also, as the feed concentration of CO_2, the more permeable component in the mixture, increases, the total amount of gas transferred from the residue to permeate stream increases, and therefore stage cut increases.

Figure 8 presents the effect of feed flow rate and CO_2 feed composition on temperature difference between the feed and residue streams. The simulation conditions are the same as those used to generate Figure 7. From Figure 8A, the temperature change across the module can be quite large (as high as 40°C) and is strongly dependent upon the concentration of CO_2 and the feed flow rate. At fixed flow rate, as CO_2 feed concentration increases, the temperature change across the module increases. At fixed feed concentration, the temperature change across the module decreases with increasing flow rate. Figure 8B shows the importance of stage cut on temperature change across the module. As stage cut increases, the temperature difference between the feed and residue ends of the module increases, as expected. However, stage cut does not provide a universal correlating parameter for these results. At the same stage cut, gas mixtures with more CO_2 in the feed experience larger temperature decreases from the feed to residue ends of the module. This result is due to the fact that changing feed composition changes not only the amount of gas that permeates across the fiber wall but also the thermodynamic properties (such as heat capacity and PVT properties) of the gas mixtures in the residue and permeate streams. While stage cut should track temperature changes that are directly proportional to the fraction of feed gas that permeates across the hollow fibers, stage cut will not capture changes in temperature due to changes in gas thermodynamic properties.

To provide an indication of the influence of the membrane on the temperature changes calculated from the feed to residue side of the membrane module, the temperature change due to Joule-Thomson expansion from feed conditions to permeate pressure was also calculated. With a feed containing 40% CO_2, the temperature decrease because of expanding the gas across an adiabatic expansion valve from 59.6 bara to 1.70 bara is 33°C. This value is somewhat less than the maximum temperature change, 40.3°C, observed in the membrane case at the highest stage cut, 53%, for which simulations are reported. If all of the gas fed to the membrane were expanded to the permeate stream (that is, 100% stage cut), the temperature difference between the residue and permeate gas would be similar to that for expanding the gas across an adiabatic expansion valve. (Bore-side pressure buildup would reduce the temperature change in a fiber relative to that in an expansion valve.) Therefore, we expect the curves in Figure 8B to go through maxima at higher stage cut before returning to values similar to the temperature change across an adiabatic expansion valve at the feed composition. The membrane both expands the gas and, at stage cuts less than 100%, selectively enriches the permeate in CO_2, which is the component (in CO_2/CH_4 mixtures) having the strongest tendency to cool upon expansion. As stage cut approaches 100%, the ability of the membrane to selectively enrich the permeate in CO_2 diminishes, and the temperature change from the high- to low-pressure side of the membrane will decrease to a value consistent with that obtained using an adiabatic expansion valve.

CO_2/CH_4 Separation: temperature-dependent permeability coefficients

For the simulation results presented in Figures 7 and 8, the gas permeability coefficients were taken to be independent of temperature in order to isolate the influence of gas-phase composition and flow rate on expansion-driven

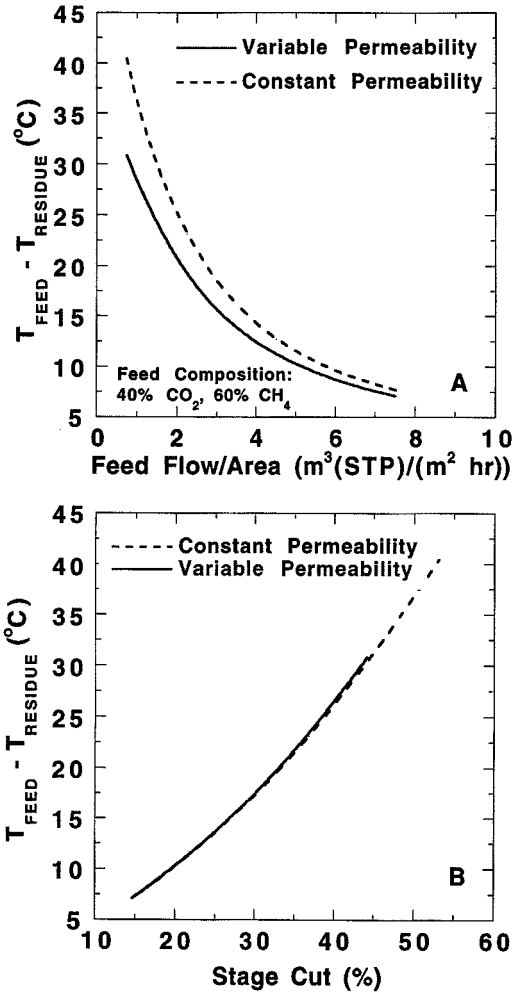

Figure 9. Temperature difference between feed and residue stream as a function of (A) feed flow rate per unit membrane area and (B) stage cut.

The simulation conditions are those for the binary natural-gas case. The solid line corresponds to simulations performed with the gas permeability coefficients set to a constant value (that is, their value at feed conditions), and the dashed line corresponds to simulations run with temperature-dependent permeability coefficients.

temperature changes. However, as the results in the previous section indicate, significant temperature changes (as high as ~ 40°C) from the feed to residue end of the module may be observed. Therefore, the binary natural-gas simulations were also performed with temperature-dependent permeability coefficients (using the activation energy of permeation values from Figure 4). These results are presented in Figure 9 for a case where the feed concentration of CO_2 is set to 40%. This case gives the largest decrease in temperature across the module of all of the cases considered. Based on the results in Figure 9A, the temperature difference between the feed and residue ends of the module at a fixed feed flow rate is lower when the permeability coefficients vary according to the temperature distribution in the module. Temperature decreases monotonically from the feed to the residue end of the module, so gas permeability coefficients also decrease from the feed to the residue end of the module (since the activation energies of permeation for these penetrants are positive (cf. Figure 4)). As an example, for the strongest temperature decrease reported in Figure 9A (approximately 41°C), the CO_2 permeability decreases by approximately a factor of 2 (from 2.2 to 1.1 Barrers) and CO_2/CH_4 selectivity nearly doubles (from 32 to 61) from the feed to residue end of the module. Thus, the amount of gas permeated (and, therefore, expanded) from the high-pressure to the low-pressure side of the membrane is significantly lower when the permeability coefficients depend on temperature. Therefore, the effect of allowing the permeability coefficients to vary with temperature is to decrease the total amount of gas that can be processed per unit area of membranes.

As shown in Figure 9B, if the results in Figure 9A are presented as a function of stage cut, the curves for constant and variable permeability practically coincide. Thus, for these simulation conditions, the most important variable for determining the temperature change is the fraction of the feed gas that is expanded into the permeate stream. That is, the changes in membrane selectivity that accompany the change in permeability coefficients with temperature do not significantly impact the enthalpy change upon expanding the gas into the permeate stream. If the selectivity were a stronger function of temperature, the coincidence of the curves in Figure 9B would not be as good since the composition of gas produced in the permeate stream would change more significantly along the module.

CO_2/CH_4 separation: five-component simulations

The previous results generated using binary CO_2/CH_4 gas mixtures demonstrate general trends for the effect of process conditions (feed flow rate and CO_2 content) on the temperature change across a module. However, real natural gas is a mixture of many components and typically includes inerts (such as N_2) and higher hydrocarbons (C_2H_6, C_3H_8, etc.) in addition to CO_2 and CH_4. An important advantage of our modeling approach is that one can easily extend it to simulate mixtures of many components. As an example, a five-component natural gas case was considered. The feed composition and module parameters are given in the cartoon in Figure 6B. The CO_2 content was set to 40%, and approximately 7% of the methane was replaced by nitrogen and higher hydrocarbons. The temperature decrease from the feed end to the residue end of the module is presented as a function of feed flow rate per unit active membrane area in Figure 10A. Results from the binary case (40% CO_2) are also included for comparison. For these multicomponent simulations, the permeability coefficients were held constant at their values at the feed conditions (that is, permeability was not allowed to vary with temperature). At the same flow rate, the temperature change in the module is less for the multicomponent case than for the binary case. This is due primarily to the smaller amount of gas that permeates from the high-pressure to the low-pressure side of the membrane in the multicomponent case. The components that replace methane are similar in permeability (N_2) or much lower in permeability (higher hydrocarbons) than methane, so the total amount of gas permeated across the membrane is lower for the multicomponent case. This effect is more easily visualized by re-

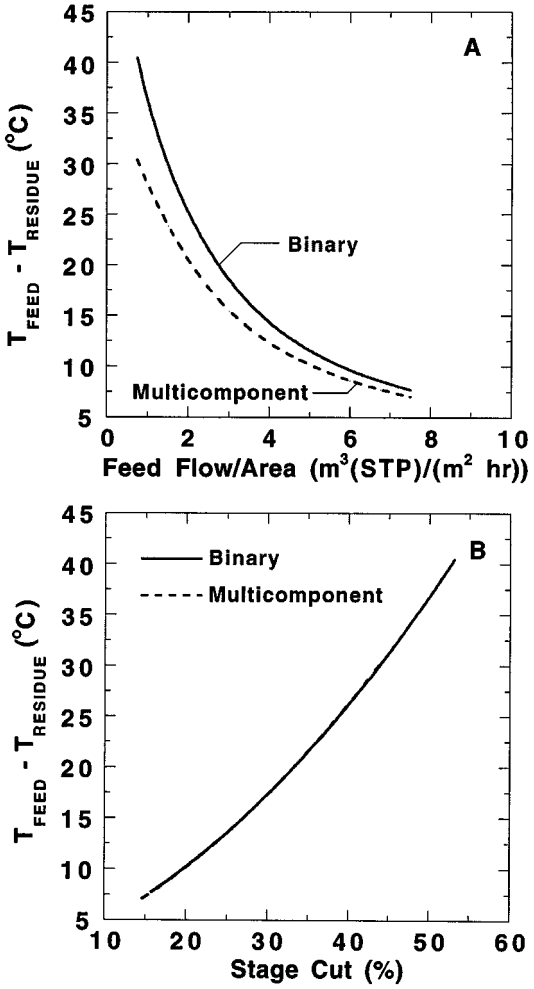

Figure 10. Temperature difference between feed and residue stream as a function of (A) feed flow rate per unit membrane area and (B) stage cut for binary natural-gas mixture and multicomponent natural-gas mixture.

Feed composition for binary mixture is 40% CO_2 and 60% CH_4. Multicomponent mixture contains 40% CO_2, 55.89% CH_4, 1.72% N_2, 1.74% C_2H_6, and 0.65% C_3H_8.

porting the temperature difference in the module as a function of stage cut, as shown in Figure 10B. From the results in this figure, the binary and multicomponent cases give essentially the same temperature change in the module at the same stage cut. Thus, the temperature changes across the module are more sensitive to stage cut than to, for example, changes in thermodynamic properties of the multicomponent mixture relative to those of the binary mixture. In this example, only about 7% of the methane in the feed was replaced with other components, and this does not appear to have an appreciable effect on gas thermodynamic properties important for calculating temperature changes in the module. If more complex gas mixtures were considered or if one or more components in the feed could condense at the conditions inside the module, the results could be significantly different from those presented in the example.

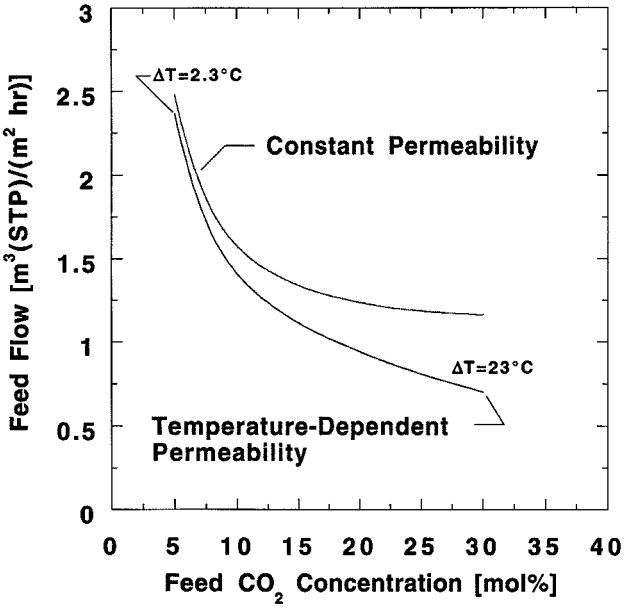

Figure 11. Effect of CO_2 concentration on amount of gas that can be processed to reach a residue composition of 2 mol % CO_2.

The simulation conditions for this natural-gas separation are given in Table 1. ΔT is the difference between the feed and residue temperatures.

CO_2/CH_4 separation: fixed-residue composition

In the series of binary CO_2/CH_4 separation simulations described in this section, the residue concentration is set to 2 mol %, consistent with pipeline specifications in the United States (Bhide and Stern, 1993a,b). The module size parameters, feed and permeate pressures, and feed temperature are given in Table 1. The composition of CO_2 in the feed is varied and the amount of gas that can be treated in one module is determined. This calculation is performed for two cases, one with the permeability coefficients set equal to their values in the feed and held constant and the other with the permeability coefficients allowed to vary with temperature according to Eq. 40. The results of this calculation are presented in Figure 11. As feed CO_2 concentration increases, the amount of gas that can be treated decreases because more CO_2 must be removed from the feed gas with a fixed amount of membrane area. The amount of gas that can be treated is higher at all feed-gas concentrations for the simulations performed with fixed values of permeability coefficients. The difference between the results for the two cases becomes greater at higher CO_2 feed concentrations. For example, at 5% CO_2 in the feed, there is less than 10% difference in the amount of feed gas that can be treated in the constant permeability case vs. the variable permeability case. However, at 30% CO_2, there is approximately a factor of 2 difference in the amount of gas that can be treated between the cases with constant permeability and temperature-dependent permeability. That is, if the effect of expansion-driven cooling of the gas mixture on the permeability coefficients is included, the amount of gas that can be treated by a single module will be approximately half the amount anticipated based on constant (that is, temperature-independent) permeability coefficients. The

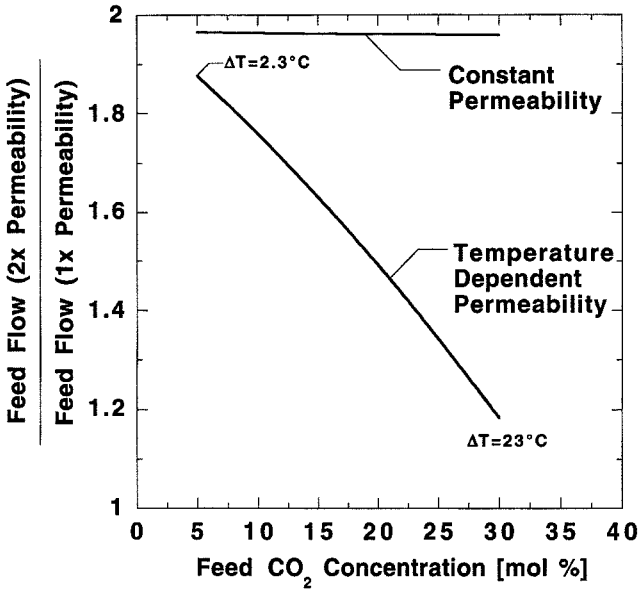

Figure 12. Effect of CO_2 concentration on the fractional increase in the amount of feed gas that can be treated with the permeance of each component doubled.

The residue composition is fixed at 2 mol % CO_2. The simulation conditions for this CO_2/CH_4 natural-gas separation are given in Table 1. The CO_2 and CH_4 permeances are set to twice the values recorded in Table 2. ΔT is the difference between the feed and residue temperatures.

temperature decrease from the feed to the residue side of the module increases markedly, from 2.3°C to 23°C, as the feed CO_2 composition goes from 5% to 30%. As the temperature decrease from the feed to the residue end of the module increases, the influence of expansion-driven cooling on permeability coefficients and, in turn, on the amount of feed gas that can be treated increases.

In the second case, the membrane thickness is reduced by a factor of 2, which has the effect of doubling the permeances of both CO_2 and CH_4. Therefore, the feed permeances of these gases are twice the values presented in Table 2. This effect should markedly increase the amount of gas that can be processed in a single module. However, the higher rates of permeation at a given feed flow rate will result in more of the feed gas being expanded into the permeate stream and, therefore, stronger effects of expansion-driving cooling on membrane performance. This effect will act to reduce the amount of feed gas that can be treated per unit membrane area. These simulations are designed to determine the interplay between these two factors.

In the simulations, the amount of gas that can be processed to reach 2% CO_2 in the residue in a single module (that is, fixed membrane area) is calculated for constant and temperature-dependent permeabilities. Figure 12 presents the ratio of feed flow rates with doubled membrane permeance to the feed flow rate with constant, nondoubled permeance as a function of feed CO_2 composition. For the constant permeability case, there is almost a doubling of the amount of feed gas that can be treated upon doubling the membrane permeances (increased bore-side pressure buildup when the permeances are doubled keeps the feed flow-rate ratio slightly less than 2). For the temperature-dependent permeability case, the feed capacity decreases strongly as the CO_2 concentration increases. At 30% CO_2, the expansion-driven cooling mitigates the doubling of permeance to such an extent that doubling the permeance only increases the amount of feed gas that can be treated by 20%. This result suggests that large gains in the feed gas throughput that might be anticipated (based on neglecting expansion-driven cooling) as a result of thinner, defect-free membranes may be markedly reduced as a result of the temperature effect for natural-gas separations.

Conclusion

A model is presented to describe temperature changes associated with expansion-driven cooling of nonideal gas mixtures as they permeate across the walls of hollow fibers in gas-separation modules. For the binary natural-gas case considered, strong temperature decreases from the feed to residue end of the module—as much as 40°C—are observed at low feed flow rates and high CO_2 concentrations in the feed. In this case, temperature changes are strongly correlated with stage cut, though there are additional effects, such as changes in gas-phase thermodynamic properties with changing feed composition, that are not captured by stage cut. The effect of expansion-driven temperature changes in membrane permeation properties reduces the stage cut at a given feed flow rate since gas permeability decreases with decreasing temperature. For the multicomponent natural-gas cases, the addition of permanent gases (that is, N_2) and hydrocarbons (ethane and propane) to mixtures of CO_2 and CH_4 results in temperature changes that are less, at the same feed flow rate, than those obtained for the binary case. This result is due primarily to the lower permeability of the additional components relative to that of CH_4. Neglecting expansion-driven cooling in natural-gas separation simulations can lead to large errors in estimating the amount of feed gas that can be treated per unit area to achieve a fixed residue composition. For 30% CO_2 feed concentration, if the effective membrane thickness is halved, only a 20% increase (rather than a factor of 2) in the amount of gas that can be treated per unit is obtained due to the impact of expansion-driven cooling.

Acknowledgments

The authors gratefully acknowledge partial support of this work by the National Science Foundation [CTS-9257911 (NSF Young Investigator Award—B.D.F.)] and CTS-9803225. We also appreciate discussions with Dr. Steve Auvil of Air Products and Chemicals, Inc. (Allentown, PA) regarding the appropriate correlation for shell-side heat-transfer coefficients and for suggesting the cases presented in Figures 11 and 12.

Notation

C_p = heat capacity (m^3/kmol)
$C_{p,F}$ = heat capacity of feed gas (m^3/kmol)
D_o = outside diameter of porous membrane support (m)
F = total feed flow rate (kmol/s)
H_j^o = ideal gas enthalpy of component j (J/kmol)
$\hat{H}_k^L$ = mixing-cup enthalpy of feed stream leaving stage k (J/kmol)
$\hat{H}_k^V$ = mixing-cup enthalpy of permeate stream leaving stage k (J/kmol)

$\hat{H}^{V}_{k-1}$ = mixing-cup enthalpy of permeate stream entering stage k from stage $k-1$ (J/kmol)
$\hat{H}^{O,V}_{k-1}$ = ideal gas mixing-cup enthalpy of permeate stream entering stage k from stage $k-1$ (J/kmol)
l = separating membrane thickness (m)
L_F = total feed flow rate (kmol/s)
M = mole-fraction-weighted average molecular weight (kg/kmol)
P_F = feed pressure (Pa)
P_P = permeate pressure (Pa)
q = conductive heat flux (W/m^2)
r = radial position (m)
R_i = hollow-fiber inside radius (m)
t = time (s)
U = internal energy (J/kmol)
V = total permeate flow rate (kmol/s)
x_{F_j} = feed mole fraction of component j
$x_{j,k}$ = residue mole fraction of component j on stage k
$y_{j,k}$ = permeate mole fraction of component j on stage k
z = axial distance along the active section of the hollow fibers measured from the residue end of the module (m)

Literature Cited

Baker, R. W., and J. G. Wijmans, "Membrane Separation of Organic Vapors from Gas Streams," *Polymeric Gas Separation Membranes*, D. R. Paul and Y. P. Yampol'skii, eds., CRC Press, Boca Raton, FL, p. 353 (1994).

Barrer, R. M., "Permeability in Relation to Viscosity and Structure of Rubber," *Trans. Faraday Soc.*, **38**, 322 (1942).

Barsaran, O. A., and S. R. Auvil, "Asymptotic Analysis of Gas Separation by a Membrane Module," *AIChE J.*, **34**, 1726 (1988).

Bhide, B. D., and S. A. Stern, "Membrane Processes for the Removal of Acid Gases from Natural Gas: I. Process Configurations and Optimization of Operating Conditions," *J. Memb. Sci.*, **81**, 209 (1993a).

Bhide, B. D., and S. A. Stern, "Membrane Processes for the Removal of Acid Gases from Natural Gas: II. Effects of Operating Conditions, Economic Parameters, and Membrane Properties," *J. Memb. Sci.*, **81**, 239 (1993b).

Bird, R. B., W. E. Stewart, and E. N. Lightfoot, *Transport Phenomena*, Wiley, New York (1960).

Boucif, N., S. Majumdar, and K. K. Sirkar, "Series Solutions for a Gas Permeator with Countercurrent and Cocurrent Flow," *Ind. Eng. Chem., Fundam.*, **23**, 470 (1984).

Coker, D. T., B. D. Freeman, and G. K. Fleming, "Modeling Multicomponent Gas Separation Using Hollow-Fiber Membrane Contactors," *AIChE J.*, **44**(6), 1289 (1998).

Cornelissen, A. E., "Heat Effect in Gas Permeation, with Special Reference to Spiral-Wound Modules," *J. Memb. Sci.*, **76**, 185 (1993).

Ghosal, K., and B. D. Freeman, "Gas Separation Using Polymer Membranes: An Overview," *Poly. Adv. Technol.*, **5**(11), 673 (1994).

Gorissen, H., "Temperature Changes Involved in Membrane Gas Separations," *Chem. Eng. Process.*, **22**, 63 (1987).

Graham, T., "On the Absorption and Dialytic Separation of Gases by Colloid Septa. Part I. Action of a Septum of Cauotchouc," *Philos. Mag.*, **32**, 401 (1866).

Haraya, K., K. Obata, T. Hakuta, and H. Yoshitome, "The Permeation of Gases Through a New Type Polyimide Membrane," *Maku (Memb.)*, **11**, 48 (1986).

Henis, J. M. S., "Commercial and Practical Aspects of Gas Separation Membranes," *Polymeric Gas Separation Membranes*, D. R. Paul and Y. P. Yampol'skii, eds., CRC Press, Boca Raton, FL, p. 442 (1994).

Inyushkin, A. V., "Thermal Conductivity," *Handbook of Physical Quantities*, I. S. Grigoriev and E. Z. Meilikhov, eds., CRC Press, Boca Raton, FL, p. 419 (1997).

Kays, W. M., and A. L. London, *Compact Heat Exchangers*, 3rd ed., McGraw-Hill, New York (1984).

King, C. J., *Separation Processes*, 2nd ed., McGraw-Hill, New York (1980).

Koros, W., D. Paul, and G. Huvard, "Energetics of Gas Sorption in Glassy Polymers," *Polymer*, **20**, 956 (1979).

Kovvali, A. S., S. Vemury, K. R. Krovvidi, and A. A. Khan, "Models and Analyses of Membrane Gas Permeators," *J. Memb. Sci.*, **73**, 1 (1992).

Krovvidi, K. R., A. S. Kovvali, S. Vermury, and A. A. Khan, "Approximate Solutions for Gas Permeators Separating Binary Mixtures," *J. Memb. Sci.*, **66**, 103 (1992).

Lide, D. R., and H. V. Kehiaian, *CRC Handbook of Thermophysical and Thermochemical Data*, CRC Press, Boca Raton, FL, p. 87 (1994).

Lipscomb, G. G., "Design of Hollow Fiber Contactors for Membrane Gas Separations," *The 1996 Membrane Technology Reviews*, D. Mulloy, ed., Business Communications, Norwalk, CT, p. 23 (1996).

Naylor, R. W., and P. O. Backer, "Enrichment Calculations in Gaseous Diffusion: Large Separation Factor," *AIChE J.*, **1**, 95 (1955).

Pan, C. Y., "Gas Separation by High-Flux Asymmetric Hollow-Fiber Membrane," *AIChE J.*, **32**, 2020 (1986).

Prausnitz, J. M., *Molecular Thermodynamics of Fluid-Phase Equilibria*, Prentice Hall, Englewood Cliffs, NJ (1969).

Rautenbach, R., and W. Dahm, "Gas Permeation—Module Design and Arrangement," *Chem. Eng. Process.*, **21**, 141 (1987).

Reid, R. C., J. M. Prausnitz, and B. E. Poling, *The Properties of Gases and Liquids*, McGraw-Hill, New York (1987).

Smith, J. M., and H. C. V. Ness, *Introduction to Chemical Engineering Thermodynamics*, 4th ed., McGraw-Hill, New York (1987).

Smith, S. W., B. D. Freeman, C. K. Hall, and R. Rautenbach, "Analytical Gas-Permeation Models for Binary Gas Mixture Separation Using Membrane Modules," *J. Memb. Sci.*, **118**, 289 (1996).

Weller, S., and W. A. Steiner, "Fractional Permeation Through Membranes," *Chem. Eng. Prog.*, **46**, 585 (1950).

Whitaker, S., *Fundamental Principles of Heat Transfer*, Krieger, Malabar, FL (1985).

Wunderlich, W., "Physical Constants of Poly(methyl methacrylate)," *Polymer Handbook*, 3rd ed., J. Brandrup and. E. H. Immergut, eds., Wiley, New York, p. V/77 (1989).

Appendix A: Order of Magnitude of Viscous Dissipation and Reversible Work Contributions to Energy Balance

Viscous dissipation

To estimate the order of magnitude of viscous dissipation on the thermal energy balance, we calculate the magnitude of the temperature change associated with viscous dissipation for steady, axial, laminar flow in a tube. In this case, the influence of viscous dissipation on enthalpy is given by the following form of the thermal energy balance (Eq. 1):

$$\rho v_z \frac{\partial H}{\partial z} = \overline{\nabla \boldsymbol{v}} : \bar{\boldsymbol{\tau}}. \tag{A1}$$

For a Newtonian fluid of constant viscosity, the viscous dissipation term for laminar tube flow is (Whitaker, 1985)

$$\overline{\nabla \boldsymbol{v}} : \bar{\boldsymbol{\tau}} = \mu \left(\frac{\partial v_z}{\partial r} \right)^2. \tag{A2}$$

For laminar flow in a tube, the righthand side of Eq. A2 is (Bird et al., 1960)

$$\mu \left(\frac{\partial v_z}{\partial r} \right)^2 = 256 \frac{\mu \langle v_z \rangle^2}{D_i^4} r^2. \tag{A3}$$

where $\langle v_z \rangle$ is average axial velocity.

For this order-of-magnitude estimate, we neglect the effects of changing composition on enthalpy and write the en-

thalpy as (Whitaker, 1985)

$$\rho\frac{\partial H}{\partial z}=\rho C_p\frac{\partial T}{\partial z}+(1-T\beta)\frac{\partial P}{\partial z}, \tag{A4}$$

where β is the isobaric thermal-expansion coefficient, which is defined as follows (Whitaker, 1985):

$$\beta=-\frac{1}{\rho}\left(\frac{\partial\rho}{\partial T}\right)_p. \tag{A5}$$

A rough indication of the magnitude of the effect of viscous dissipation on flow can be estimated by inserting Eqs. A2, A3, and A4 into Eq. A1 and neglecting the effect of pressure changes on temperature. The result is

$$\left(\frac{\partial T}{\partial z}\right)_{\substack{\text{viscous}\\ \text{dissipation}}}=\frac{32\langle v_z\rangle\mu}{\rho C_p D_i^2}\frac{(2r/D_i)^2}{1-(2r/D_i)^2}$$

$$=32\,Re\frac{\nu^2}{C_pD_i^3}\frac{(2r/D_i)^2}{1-(2r/D_i)^2}. \tag{A6}$$

According to Whitaker, an order of magnitude analysis of Eq. A6 suggests that the order of magnitude of the temperature gradient owing to viscous dissipation is (Whitaker, 1985)

$$O\left(\left(\frac{\partial T}{\partial z}\right)_{\substack{\text{viscous}\\ \text{dissipation}}}\right)=32\,Re\frac{\nu^2}{C_pD_i^3}. \tag{A7}$$

In the cases presented in this work, shell-side feed is used. To calculate the impact of viscous dissipation on the temperature gradient on the bore side of the membrane, the diameter in Eq. A7 is replaced by the hydraulic diameter, D_H, and the appropriate Reynolds number is the shell-side Reynolds number, Re_s. In order to calculate Reynolds number, the hydraulic diameter is required. To calculate hydraulic diameter, the module void fraction, ψ, must be calculated. The module outside diameter, D_{OM}, is taken to be 12 in. [0.3048 m], which is typical for industrial separators used for natural-gas purification. Typically, a collection tube of diameter D_{IM} runs axially along the center of the module for feed distribution in shell-side feed and for permeate collection in bore-side feed. The diameter of the collection tube is set to 2 in. [0.0508 m]. The module void fraction may be calculated from the following equation:

$$\psi=1-\frac{\text{Vol. of fibers}}{\text{Vol. of module}}=1-N_F\frac{\left[2(R_o+l)\right]^2}{D_{OM}^2-D_{IM}^2}. \tag{A8}$$

For a module with 500,000 fibers and an outside fiber radius of 150×10^{-6} m, the void fraction is 0.50. The hydraulic diameter is given by (Bird et al., 1960)

$$D_H=4\left(\frac{R_o+l}{2}\right)\frac{\Psi}{1-\Psi}. \tag{A9}$$

For fibers with an outside radius of 150×10^{-6} m and a void fraction of 0.50, the hydraulic diameter is 300×10^{-6} m. The shell-side Reynolds number, Re_s, is calculated as follows (Whitaker, 1985):

$$Re_s=\frac{2(R_o+l)G_s}{\mu_s}, \tag{A10}$$

where μ_s is the gas-mixture viscosity, and G_s is the mass flow rate per unit cross-sectional area of the module available for flow. For example, for pure CO_2 at a feed flow rate of 50,000 SCFH [0.3933 m^3(STP)/s], G is 10.9 kg/(m^2·s). If the gas is assumed to have the thermodynamic properties of carbon dioxide at 50°C and 1 atm pressure, then the viscosity is 16.035×10^{-6} Pa·s, and the Reynolds number is approximately 200. The gas heat capacity (in the limit of low pressure) is 880 J/(kg·K) (Lide and Kehiaian, 1994). The kinematic viscosity of CO_2 at 50°C and 1 atm is 9.662×10^{-6} m^2/s (Whitaker, 1985). Therefore, the order of magnitude of the temperature gradient due to viscous dissipation is 0.26°C/cm. This temperature change is of the same order of magnitude as the temperature changes observed due to expansion-driven changes in gas temperature. However, as described below, the effect of viscous dissipation is largely offset by an equivalent decrease in temperature due to reversible work.

Reversible work

To estimate the impact of reversible work on the thermal energy balance, we estimate the magnitude of the temperature gradient associated with reversible work for steady, axial, laminar flow in a tube. We neglect the effect of viscous dissipation and heat conduction and write the thermal energy balance (Eq. 1) as follows:

$$\rho\frac{\partial H}{\partial z}=\frac{\partial P}{\partial z}. \tag{A11}$$

The pressure gradient for laminar tube flow is (Whitaker, 1985)

$$\frac{\partial P}{\partial z}=-32\frac{\mu\langle v_z\rangle}{D_i^2}. \tag{A12}$$

Inserting Eqs. A4 and A12 into A11 gives

$$\left(\frac{\partial T}{\partial z}\right)_{\substack{\text{reversible}\\ \text{work}}}=-32\frac{\mu\langle v_z\rangle}{\rho C_pD_i^2}T\beta=-32\,Re\frac{\nu^2}{C_pD_i^3}T\beta. \tag{A13}$$

For an ideal gas, the compressibility coefficient is equal to $1/T$, and the expression for reversible work becomes

$$\left(\frac{\partial T}{\partial z}\right)_{\substack{\text{reversible}\\ \text{work}}}=-32\,Re\frac{\nu^2}{C_pD_i^3}. \tag{A14}$$

As for viscous dissipation, for the shell-side feed cases of interest in this work, the appropriate Reynolds number in Eq.

A14 is the shell-side Reynolds number, and the appropriate diameter is the hydraulic diameter. This term has the same order of magnitude as the viscous dissipation (Eq. A7), but is opposite in sign. That is, the temperature gradient due to reversible work for the flow conditions described earlier is -0.26°C/cm if the gas behaves ideally. As gas travels along the fibers, it is heated as a result of viscous dissipation and cooled as a result of reversible work. Within the scope of this order-of-magnitude analysis, these two effects cancel one another. Therefore, in the remainder of the analysis of the thermal energy balance, we neglect both effects.

A deeper analysis should consider the impact of nonideal gas behavior on reversible work and the effect of the permeable fiber walls on both the reversible work and viscous dissipation. Using the Redlich-Kwong equation of state, the product βT can be evaluated analytically. The result is

$$\beta T = \frac{\dfrac{R}{\hat{V}-b} + \dfrac{a}{2T^{3/2}\hat{V}(\hat{V}+b)}}{\dfrac{R}{\hat{V}-b}\left[\dfrac{\hat{V}}{\hat{V}-b}\right] - \dfrac{a}{T^{3/2}\hat{V}(\hat{V}+b)}\left[\dfrac{2\hat{V}+b}{\hat{V}+b}\right]}, \quad \text{(A15)}$$

where a and b are parameters from the Redlich-Kwong equation of state, $\hat{V}$ is the molar volume of the gas, and R is the gas constant. The value of βT for a mixture of CO_2 and CH_4 at 50°C and 59.6 bar (the feed conditions for our natural gas purification simulations) is 1.6 when the CO_2 concentration is 40 mol. %, which is the highest value considered in these simulations. In this case, the absolute value of the reversible work term will be larger than that due to viscous dissipation, and the net temperature change along the shell side of the fibers will be -0.15°C/cm. This is a conservative (that is, high) estimate of the absolute value of the magnitude of this effect because, as the gas travels along the fibers, the residue side flow rate decreases due to permeation into the bore of the fibers. As the flow rate decreases, the importance of these effects is diminished. However, in the case of nonideal gas mixtures, these effects are strong enough that they warrant further study. It would be particularly interesting to understand better, perhaps using a more elaborate two- or three-dimensional model of the fluid mechanics, mass transfer, and heat transfer in a module, the detailed impact of viscous dissipation and reversible work on temperature profile in modules. However, such an analysis is not possible within the scope of the one-dimensional model described in this work.

Appendix B: Heat-Transfer Model for Hollow Fiber Wall

In this Appendix, a model is provided to estimate the overall heat-transfer coefficient for the wall of the hollow fibers. In this regard, Figure B1 presents a cartoon of the cross section of a hollow fiber. The steady-state heat transfer from the shell side of the fiber to the bore of the fiber is modeled as a series of four resistances: (1) bore side boundary layer; (2) porous fiber support; (3) dense separating layer of the membrane; and (4) shell side boundary layer. In terms of these

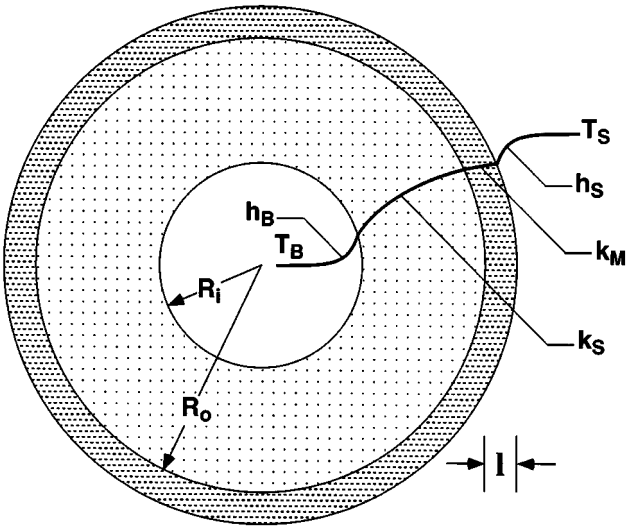

Figure B1. Fiber cross section for heat-transfer-resistence model.

resistances, the overall heat-transfer coefficient (based on outside area) defined in Eq. 22 is given by (Whitaker, 1985)

$$U_o = \left[\frac{1}{h_B}\frac{(R_o+l)}{R_i} + \frac{R_o}{k_s}\frac{(R_o+l)}{R_o}\ln\left(\frac{R_o}{R_i}\right) + \frac{(R_o+l)}{k_M}\ln\left(\frac{R_o+l}{R_o}\right) + \frac{1}{h_S}\right]^{-1} \quad \text{(B1)}$$

where h_B and h_S are the heat-transfer coefficients associated with the bore side and shell side boundary layer resistances to heat transfer, respectively. The inner and outer radii of the porous hollow fiber support are R_i and R_o, respectively. The thickness of the membrane separating layer is l. The thermal conductivities of the support layer and separating layer are k_S and k_M, respectively. The bulk or mixing-cup temperatures of the gas in the bore of the fibers and on the shell side of the fibers are T_B and T_S, respectively.

For calculations of the bore- and shell-side resistances to heat transfer, there are no available heat-transfer correlations specifically derived for hollow fibers used in gas separations. Therefore, in the following analysis, we use heat-transfer correlations originally derived for heat exchangers, that is, impermeable tubes. In our earlier studies of pressure distribution in hollow fibers (Coker et al., 1998), we showed that for typical operating conditions, the fiber wall permeability did not influence the velocity profiles enough to invalidate the use of Poiseuille's law, which was derived for impermeable tubes. In the same spirit, we use heat-transfer correlations derived for impermeable tubes as a first approximation in the analysis of the gas-phase resistances to heat transfer.

The bore-side boundary-layer resistance is modeled using the following solution to the Graetz problem for heat transfer to fluids in laminar flow in long tubes (Whitaker, 1985):

$$h_B = 3.66 \frac{k_{G,B}}{2R_i}, \qquad \text{(B2)}$$

where $k_{G,B}$ is the average thermal conductivity of the gas in the bore of the fibers at a particular location in the fibers. For flow rates of interest in typical industrial applications, the product of the Reynolds number and Prandtl number are sufficiently low to make Eq. B2 valid for all of the gas flow rates considered in this study. If $(Re_B Pr_B R_i/L)^{1/3}$ is greater than 1, an additional term is added to Eq. B2. This correction is provided in the literature (Whitaker, 1985). Re_B and Pr_B are the bore-side Reynolds number and Prandtl number, respectively, and L is the fiber length. In practice, Eq. B2 should be valid for most cases of practical interest. Since the gas composition varies along the fibers, $k_{G,B}$ will change, which will change h_B. For the purposes of this estimate, since the thermal conductivity of the gases considered in these simulations (such as CO_2 and CH_4) are similar, we treat h_B as a constant with its value set based on the gas composition in the feed to the module. If desired, of course, the value of h_B could be computed locally along the fiber length and used in the calculation of U_o.

To provide an estimate of the resistance to heat transfer resulting from the bore-side boundary layer, Table B1 was prepared. In this table, the bore-side resistance is calculated for several limiting cases of temperature and pressure. Limiting cases in composition (that is, 100% CO_2 and 100% CH_4) and pressure (atmospheric and 100 bar) are considered. These conditions bracket the simulation conditions used in this study. The inside fiber radius was taken to be 75×10^{-6} m, and the outside fiber radius, $R_o + l$, was taken to be 150×10^{-6} m. These values were used throughout this study and are representative of current industrial modules. The resistance to heat transfer is of the order of several hundred W/(m^2·K).

The resistance to heat transfer in the porous support of the hollow fiber was modeled as a one-dimensional solid polymer matrix containing continuous channels connecting the bore side of the porous support to the membrane side of the support. Accordingly, the effective thermal conductivity of the support, k_S, is given by the following approximation:

$$k_S = \phi_P k_P + (1-\phi_P) k_{G,B}, \qquad \text{(B3)}$$

where k_P is the polymer thermal conductivity, and ϕ_P is the volume fraction of polymer in the porous support. Current industrial hollow fibers have a porosity of approximately 50%, so ϕ_P was set to 0.5. Based on a polymer thermal conductivity value of 0.2 W/(m K), which is typical for poly(methylmethacrylate), a common glassy polymer (Wunderlich, 1989), and the extremes in the gas thermal conductivity values presented in Table B1, the range for the resistance to heat transfer of the porous support is

$$1{,}050 < \frac{k_S}{(R_o + l)\ln(R_o/R_i)} < 1{,}320 \text{ W/(m}^2\text{·K)}. \qquad \text{(B4)}$$

This resistance is smaller than the gas-phase resistance in the bore side of the hollow fibers.

The heat-transfer resistance of the separating membrane layer is estimated assuming a separating layer thickness, l, of 0.1×10^{-6} m and a membrane thermal conductivity of 0.2 W/(m K). In this case, the heat-transfer resistance is

$$\frac{k_M}{(R_o + l)} \frac{1}{\ln(1 + l/R_o)} \approx \frac{k_M}{l} = 2\times10^6 \text{ W/(m}^2\text{·K)} \qquad \text{(B5)}$$

and clearly offers no significant resistance to heat transfer.

To estimate the heat-transfer resistance to the shell-side of the hollow fibers, the following correlation is used:

$$h_S = \frac{k_{G,S}}{2(R_o + l)} \left[3.66 + 1.077\left(Re_S Pr_S (R_o + l)/D_H\right)^{1/3}\right], \qquad \text{(B6)}$$

where $k_{G,S}$ is the average thermal conductivity of the gas on the shell side of the fibers, and D_H is the hydraulic diameter of the shell side of the module in meters. The Reynolds and Prandtl numbers of the gas on the shell side of the fibers are Re_S and Pr_S, respectively, and the hydraulic diameter of the shell is D_H. This correlation was kindly provided by Dr. Steve Auvil of Air Products and Chemicals, Inc. (Allentown, PA) and is based on numerical solutions of the governing momentum, mass, and heat-transfer equations in a model of an industrial gas separation module.

For this order of magnitude estimate, we estimate the gas physical properties at 59.6 bar and 50°C, which are the feed temperature and pressure used in these simulations. For this particular example, the feed-gas composition is 40% CO_2 and 60% CH_4. The heat capacity of this gas mixture was estimated, using the Lee-Kesler method, to be 45,800 J/(kmol·K) (Reid et al., 1987). The thermal conductivity of the mixture, based on linear interpolation using the values in Table B1, is 47×10^{-3} W/(m·K). The feed flow rate is 50,000 SCFH [0.3933 m^3(STP)/s], so G is 6.72 kg/(m^2·s) if the values of D_{OM} and D_{IM} are 0.3048 m and 0.0508 m, respectively. As indicated in Appendix A, the shell-side Reynolds number is approximately 149 and the hydraulic diameter is 300×10^{-6} m for this case. Based on these estimates, the shell side convective heat-transfer coefficient is estimated from Eq. B6 to be 1,130 W/(m^2·K).

The largest resistances to heat transfer across the fiber wall are the heat-transfer resistances in the gas-phase boundary layers and in the membrane support. For the example considered in this Appendix, the membrane layer of the hollow fiber offers negligibly a very small contribution to the overall resis-

Table B1. Bore-Side Boundary-Layer Resistance to Heat Transfer

Gas	$k_{G,B}\times10^3$ [W/(m·K)]*	h_B [W/(m^2·K)]	$h_B[R_i/(R_o + l)]$ [W/(m^2·K)]
1 bar, 50°C			
CO_2	18.4	448	224
CH_4	37.6	917	458
100 bar, 50°C			
CO_2	74.4	1,815	908
CH_4	47.7	1,164	582

*Gas thermal conductivity data from Inyushkin (1997).

tance, so that U_o can be written as follows:

$$U_o \approx \left[\frac{1}{h_B} \frac{(R_o + l)}{R_i} + \frac{R_o}{k_S} \frac{(R_o + l)}{R_o} \ln \frac{R_o}{R_i} + \frac{1}{h_S} \right]^{-1}$$

$$\approx \left[\frac{1}{h_B} \frac{R_o}{R_i} + \frac{R_a}{k_s} \ln \left(\frac{R_o}{R_i} \right) + \frac{1}{h_S} \right]^{-1}. \quad \text{(B7)}$$

Based on the values for these contributions, the overall heat-transfer coefficient should have a value of the order of several hundred W/(m^2·K).

To estimate the importance of the overall heat-transfer coefficient on the temperature distribution in the module, the number of transfer units (NTU) is defined as follows (Kays and London, 1984):

$$\text{NTU} = \frac{U_o A}{(LC_p)_{\min}}, \quad \text{(B8)}$$

where A is the total surface area of the membrane module, and $(LC_p)_{\min}$ is the minimum value of the product of flow rate and heat capacity. As NTU increases, the efficiency of heat transfer across the fiber wall increases (that is, the amount of heat exchanged between the residue and permeate sides of the fibers approaches the maximum amount allowed based on thermodynamic constraints). For the conditions considered in this study, NTU is sufficiently high that the fiber wall behaves as an essentially infinitely conductive heat-transfer surface. A calculation of the NTU of the feed, permeate, and residue streams for the binary natural-gas case discussed in this study gives the following order for the NTU values:

$$\text{NTU}_{\text{Feed}} < \text{NTU}_{\text{residue}} < \text{NTU}_{\text{permeate}}.$$

For the particular case when the feed flow rate is 2,639 m^3(STP)/h and the feed concentration is 40% CO_2, the NTU value of the feed stream is approximately 72 and that of the permeate is approximately 135 [U_o = 290 W/(m^2·K); A = 377 m^2; flow rate = 1,416 m^3(STP)/h]. For a countercurrent heat exchanger, a value of NTU of 30 means that the exchanger efficiency is at least 97%, which means that the amount of energy exchanged between the permeate and residue streams would be at least 97% of the maximum possible energy exchange (Kays and London, 1984). Since the NTU values in our studies for even the highest flow rates are substantially higher than this, it is a good approximation to assume that the fiber wall is essentially infinitely conductive. Therefore, at a given axial position in the module, the local residue temperature is practically equal to the local permeate temperature. Based on these considerations, all of the simulation results reported in this study were obtained with U_o set to 1,000 W/(m^2·K). When the overall heat-transfer coefficient was varied from 290 W/(m^2·K) to 1,000 W/(m^2·K), there was no significant difference in the temperature profiles over the range of flow rates and simulation conditions considered.

Manuscript received Dec. 21, 1998, and revision received Apr. 26, 1999.